Supporting Information

Experimental Section:

Materials: Cesium chloride (CsCl, 99.9%), sodium chloride (NaCl, 99.8%), silver chloride (AgCl, 99.8%), bismuth chloride ($BiCl_3$, 99.9%), hydrochloric acid (HCl, ACS reagent, 37 wt.% in water), and isopropanol were purchased from Aladdin. All the above chemical reagents were used directly and without any purification.

Synthesis of $Cs_3Bi_2Cl_9$ Single Crystals: CsCl (505.1mg, 3.0mmol), and $BiCl_3$ (630.7mg, 2.0mmol) were dissolved in 6 mL HCl with a 10 mL Teflon liner. Then, the container was transferred to a stainless-steel Parr autoclave and heated at 160 °C for 10 h. After the reaction, the solution was slowly cooled to room temperature at a rate of 1.5 °C h^{-1}. The obtained SCs were filtered out, washed with isopropanol, and then dried at 60 °C for 1 h in an oven.

Synthesis of $Cs_2AgBiCl_6$ Single Crystals: CsCl (505.1mg, 3.0mmol), AgCl (215.0mg 1.5mmol) and $BiCl_3$ (473.0mg, 1.5mmol) were dissolved in 38 mL HCl with a 50 mL Teflon liner. Then, the container was transferred to a stainless-steel Parr autoclave and heated at 160 °C for 10 h. After the reaction, the solution was slowly cooled to room temperature at a rate of 1.5 °C h^{-1}. The obtained SCs were filtered out, washed with isopropanol, and then dried at 60 °C for 1 h in an oven.

Synthesis of $Cs_2NaBiCl_6$ Single Crystals: CsCl (505.1mg, 3.0mmol), NaCl (87.6mg 1.5mmol) and $BiCl_3$ (473.0mg, 1.5mmol) were dissolved in 38 mL HCl with a 50 mL Teflon liner. Then, the container was transferred to a stainless-steel Parr autoclave and heated at 160 °C for 10 h. After the reaction, the solution was slowly cooled to room temperature at a rate of 1.5 °C h^{-1}. The obtained SCs were filtered out, washed with isopropanol, and then dried at 60 °C for 1 h in an oven.

Preparation of single-crystal devices: A couple of gold pastes was deposited on both the top and bottom of the Cs_2BBiCl_6 (B =Ag, Na) SCs (along the (011) plane) to form the structure of Au/ Cs_2BBiCl_6 (B =Ag, Na) SC/Au. Similarly, A couple of gold pastes were deposited on one crystal plane as electrodes of $Cs_3Bi_2Cl_9$.

Measurements and characterizations: The PXRD measurement method involved

grinding the SCs into powders in a mortar, XRD patterns of the products were recorded with an X-ray diffractometer (Empyrean) using Cu Kα radiation and a PIVcel3D 2 × 2 area detector, operating at 40 KV and 40 mA. The diffraction patterns were collected under ambient conditions using a parallel beam geometry and the symmetric reflection mode. XRD data analysis was elaborated using the MDI Jade 6 software. The UV-vis absorption spectrum was measured on an ultraviolet-visible-infrared spectrophotometer (UV 3600) with an integrating sphere. The PL spectrum was measured using a Fluoromax-4 fluorescence spectrophotometer excited by 365 nm output of a continuous xenon lamp (Xe 900). The excitation slit width was set at 15 nm, the detection slit width was set at 10 nm, and the spectra were recorded with 2 nm steps. The temperature-dependent PL spectra were carried out using a fluorescence spectrometer (PL-TCSPC) excited by 365nm from 80K to 200K. The time-resolved photoluminescence (TRPL) measurement was performed using a fluorescence spectrometer (PL-TCSPC). X-ray photoelectron spectroscopy (XPS) was carried out with a Thermo Fisher Scientific ULTRA-DLD spectrometer using a monochromatic Al Kα source, operated at 20 mA and 15 KV. Spectra have been charge-corrected to the main line of the carbon 1s spectrum (adventitious carbon) set to 284.8 eV and spectra were analyzed using Avantage software. TGA was performed using a TA differential scanning calorimetry and thermogravimetric analyzer (SDT Q600) at a heating rate of 10℃min-1from room temperature to 800 °C in N_2 flow using an alumina crucible.

Calculation methods: All of the first principle calculations were based on the Vienna Ab initio Simulation Package (VASP). The interaction between ions and valence electrons was described by Projected Augmented Wave (PAW), and the exchange-correlation interaction was described by the Perdew-Burke-Ernzerhof generalized gradient approximation (PBE-GGA). The cut-off energy was set as 450 eV, and the convergence criteria for self-consistent electronic energy and residual force were respectively assumed to be 10-5 eV/atom and 0.02 eV/Å, which could ensure sufficient accuracy. The k points are set 2 × 2 × 2 based on Monkhorst-Pack meshes for Cs2BiNaCl6 in Fm"-3"m phases, respectively. For band structure calculations, the

paths of the Brillouin zone were set up based on previous work, and the results of the band gaps SOC (Spin Orbit Coupling) and without SOC were obtained by using the VASPKIT.

X-ray detection performance: For X-ray detection measurements, a tungsten anode X-ray tube (Amptek Mini-X2) was used as the X-ray source. The X-ray tube voltage was adjusted from 35 kV to 70 kV, and the current was adjusted from 5 to 200 μA to change the dose rate of the X-rays. To complete the X-ray response at lower dose rates, we use aluminum foil to block the radiation and accurately calibrated the corresponding dose rates.During the measurements, the X-ray response current was collected using a precision source meter (Keithley 6517B).

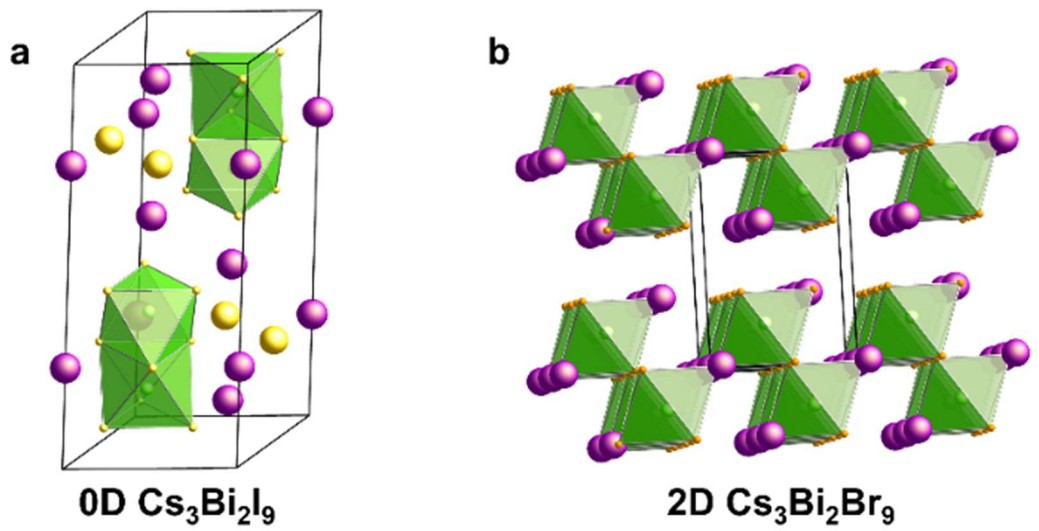

Figure S1. Crystal structure of (a) 0D $Cs_3Bi_2I_9$ and (b) 2D $Cs_3Bi_2Br_9$. The unique double octahedron of $Cs_3Bi_2I_9$ connected in a face-to-face manner is separated by a large volume of Cs ions, forming a 0D structure.$Cs_3Bi_2Br_9$, due to the smaller volume of halogen atoms, gives rise to a laminar 2D structure with corner-to-corner connections.

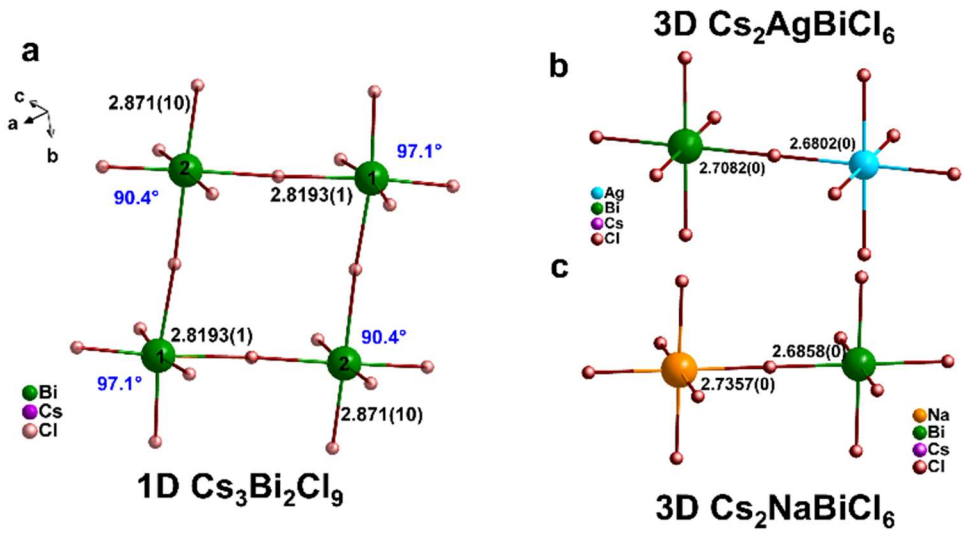

Figure S2. Coordination diagrams of (a) $Cs_3Bi_2Cl_9$[1], (b) $Cs_2AgBiCl_6$ and (c) $Cs_2NaBiCl_6$. In the four neighboring $BiCl_6$ octahedra of $Cs_3Bi_2Cl_9$, there are two Bi elements with different chemical environments, which are represented by the same bond angles as well as bond lengths. The order of chemical bond lengths in double perovskite is as follows: Ag-Cl < Bi-Cl ($Cs_2NaBiCl_6$) < Bi-Cl ($Cs_2AgBiCl_6$) < Na-Cl. The length of a chemical bond is a direct reflection of the bond energy.

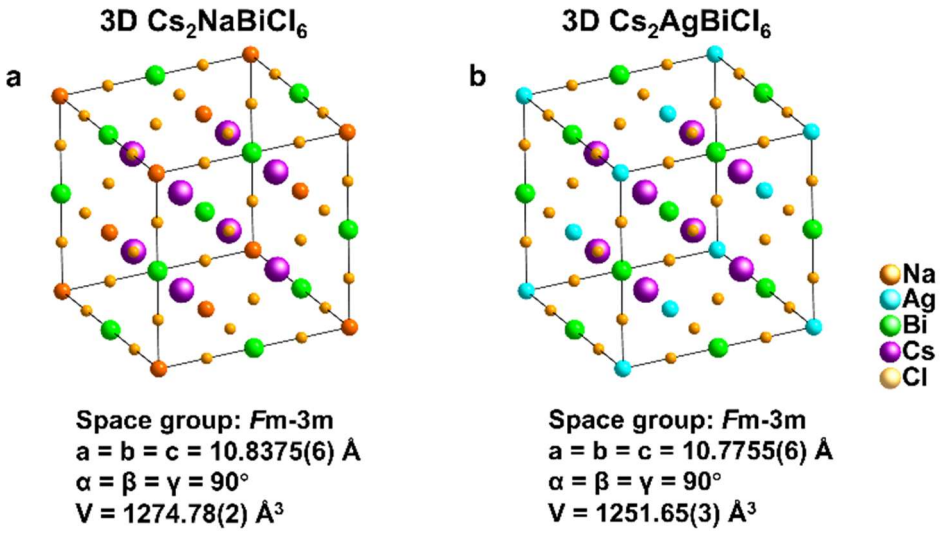

Figure S3. The unit cells and paraments of (a) $Cs_2NaBiCl_6$[2] and (b) $Cs_2AgBiCl_6$[3].

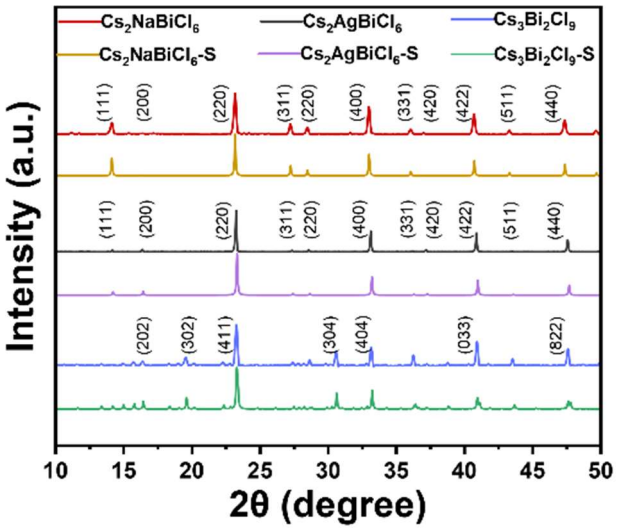

Figure S4. Power XRD patterns of $Cs_3Bi_2Cl_9$, $Cs_2AgBiCl_6$ and $Cs_2NaBiCl_6$.

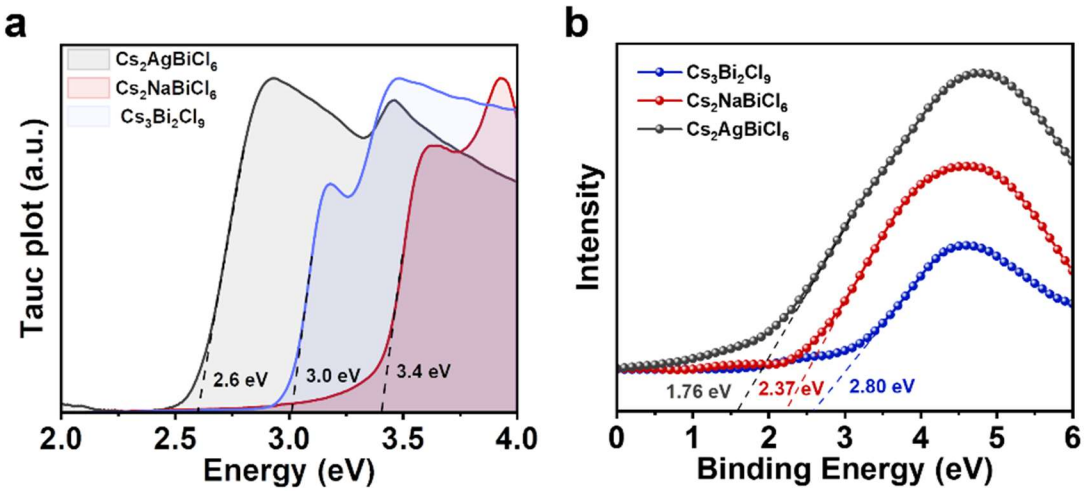

Figure S5. (a) Normalized Tauc plots of $Cs_3Bi_2Cl_9$, $Cs_2AgBiCl_6$ and $Cs_2NaBiCl_6$. (b) XPs Valence band spectra of $Cs_3Bi_2Cl_9$, $Cs_2AgBiCl_6$ and $Cs_2NaBiCl_6$.[4-6]

Table S1 The bandgap (E_g), valence band (E_v) and conduction band (E_c) correspond to the energy.

	E_g (eV)	E_v (eV)	E_c (eV)
$Cs_2AgBiCl_6$	2.6	1.76	-0.84
$Cs_2NaBiCl_6$	3.4	2.37	-1.03
$Cs_3Bi_2Cl_9$	3.0	2.80	-0.20

Table S2. Elemental analysis by Inductively Coupled Plasma (ICP).

Element	Weight %	Atomic %	Ratio
Cs	32.5	0.245	2
Na	2.96	0.128	1
Bi	26.8	0.128	1

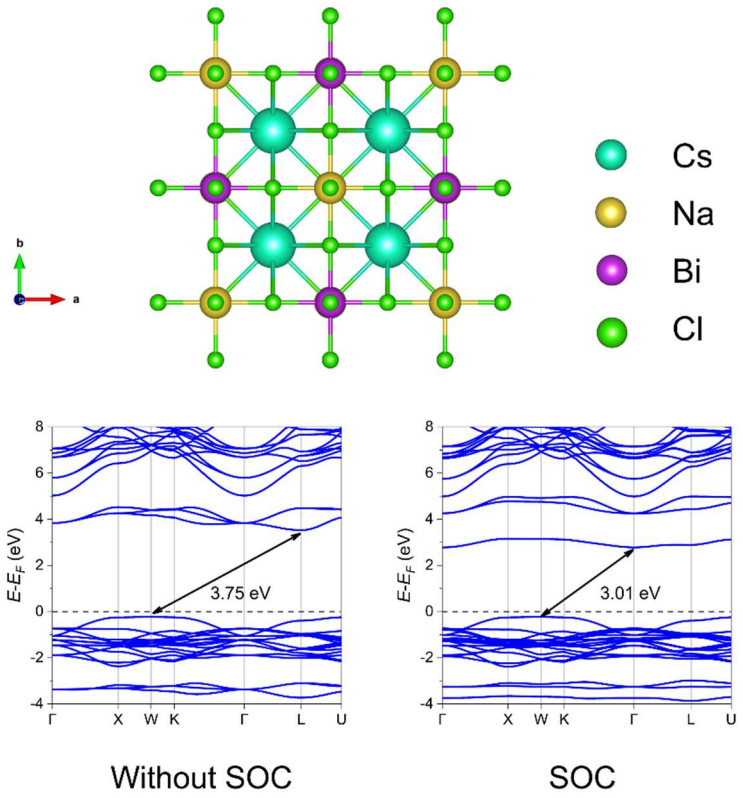

Figure S6. Electronic band structures for Cs2NaBiCl6 performed with SOC (Spin Orbit Coupling) and without SOC.

To further elucidate the optical and electronic performances of $Cs_2NaBiCl_6$, the band gap has been calculated considering SOC and without SOC. For $Cs_2NaBiCl_6$ without SOC, the valence band maximum (VBM) and conduction band minimum (CBM) are located at the W and L points, respectively. However, after considering SOC, the band

structure of $Cs_2NaBiCl_6$ remains indirect but VBM and CBM positions are changed. The indirect bandgap is reduced to 3.01 eV with the VBM and CBM located at W and Γ points, respectively. A unique intermediate band emerges above the Fermi level, which results in bandgap reduction after applying SOC. Because of the heavy atom (like Bi), SOC has a significant influence on the bandgap of $Cs_2NaBiCl_6$. The experimental bandgap value (Eg = 3.4 eV) is located between the results of theoretical calculation with SOC and that without SOC.

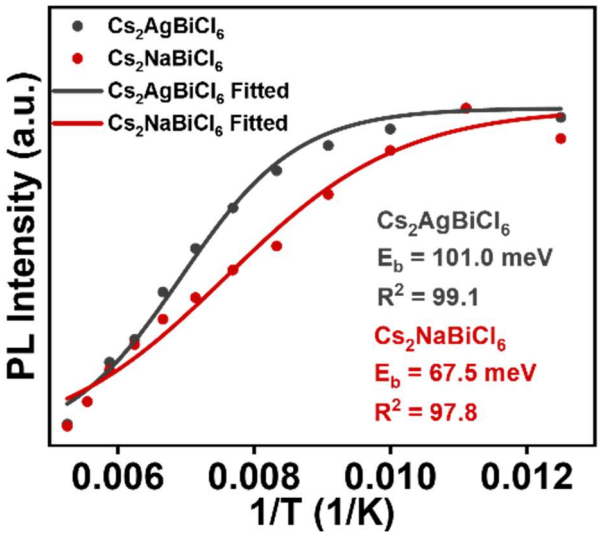

Figure S7. PL intensity as a function of temperature for $Cs_2AgBiCl_6$ and $Cs_2NaBiCl_6$. According to the temperature-dependent PL intensity, the exciton binding energy (E_b) of the two samples can be calculated by fitting the Equation:[7]

$$I(T)=\frac{I_0}{1+A\exp(-\frac{E_b}{k_bT})}$$

Where I_0 is the PL intensity at 0K, and k_B is the Boltzmann constant. $Cs_2NaBiCl_6$ has a lower exciton binding energy, which is more favorable for separation of charge.

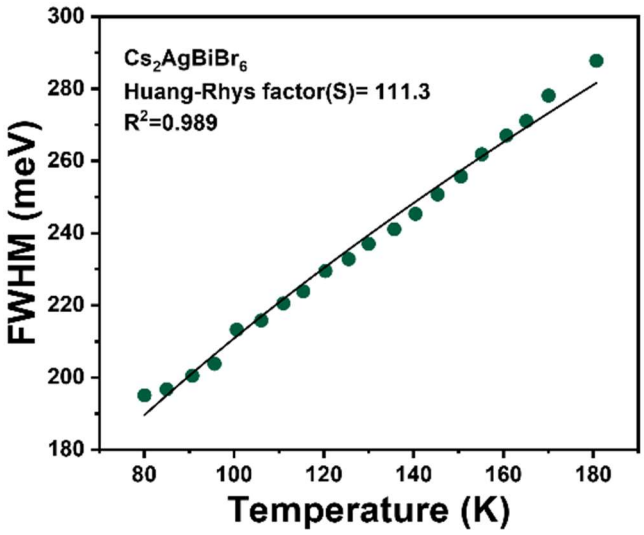

Figure S8. The FWHM as a function of temperature for $Cs_2AgBiBr_6$.[8]

Figure S9. The XPS spectra of $Cs_3Bi_2Cl_9$, $Cs_2AgBiCl_6$ and $Cs_2NaBiCl_6$.

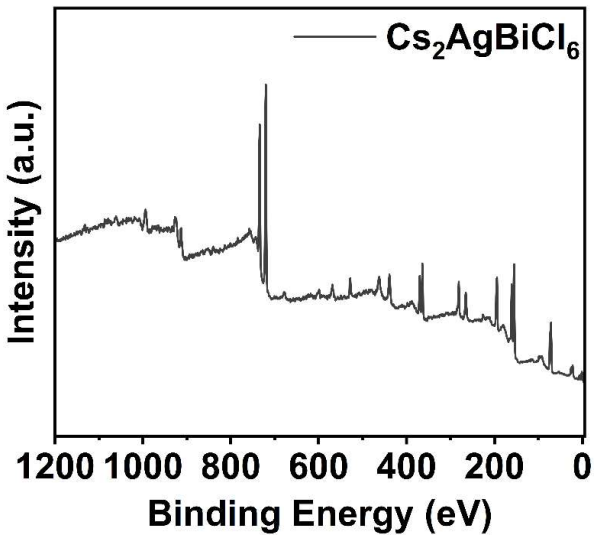

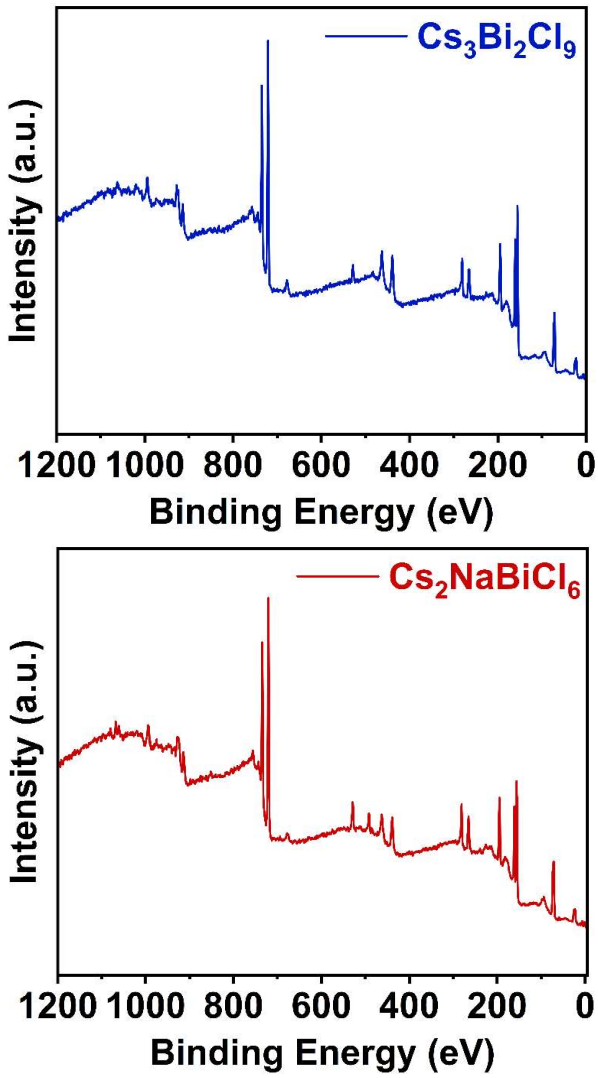

Figure S10. Device structure of $Cs_3Bi_2Cl_9$ SC detectors.

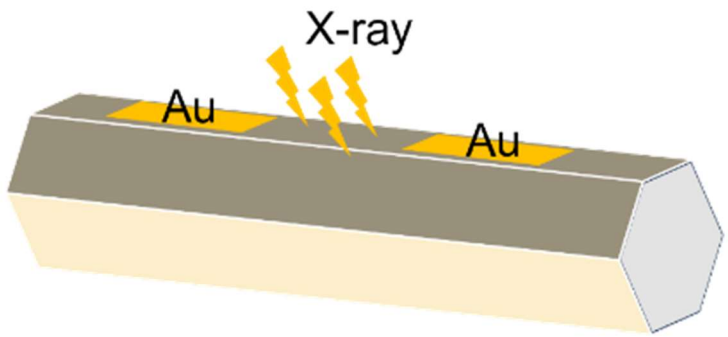

Figure S11. The photograph of single crystals and devices.

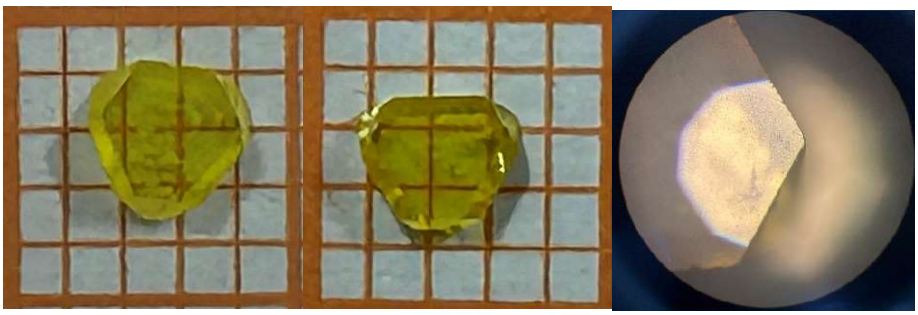

The photograph of $Cs_2AgBiCl_6$ single crystals.

The photograph of $Cs_2NaBiCl_6$ single crystals.

The photograph of $Cs_3Bi_2Cl_9$ single crystals.

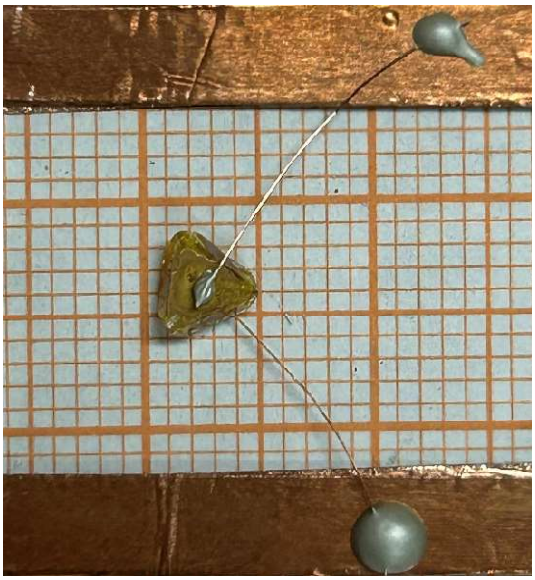

The photograph of $Cs_2AgBiCl_6$ X-ray detectors.

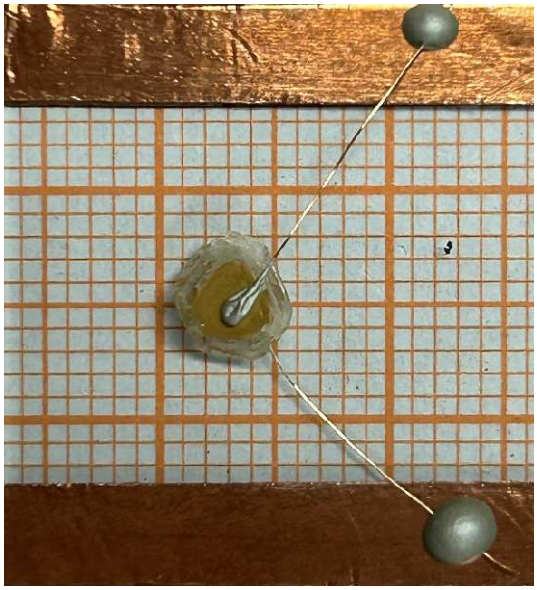

The photograph of $Cs_2NaBiCl_6$ X-ray detectors.

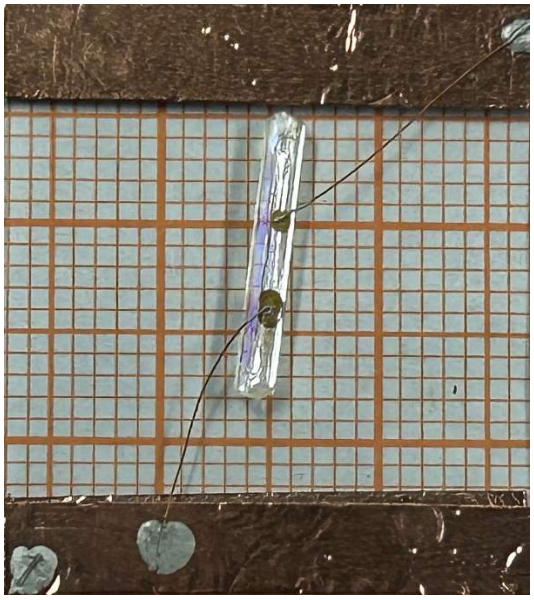

The photograph of $Cs_3Bi_2Cl_9$ X-ray detectors.

Table S3. The resistivity of $Cs_2AgBiCl_6$.

$Cs_2AgBiCl_6$	Resistivity ($\times 10^{10}$ Ω cm)
1	3.51
2	1.34
3	2.52
4	0.98
5	3.20
6	2.86

Table S4. The resistivity of $Cs_2NaBiCl_6$.

$Cs_2NaBiCl_6$	Resistivity ($\times 10^{10}$ Ω cm)
1	8.52
2	7.83
3	9.3
4	9.86
5	10.7
6	9.54

Table S5. The resistivity of $Cs_3Bi_2Cl_9$.

$Cs_3Bi_2Cl_9$	Resistivity ($\times 10^{10}$ Ω cm)
1	13.5
2	20.6
3	17.4
4	10.8
5	17.9
6	19.5

Figure S12. The I–T response curves of $Cs_2NaBiCl_6$, $Cs_3Bi_2Cl_9$, and $Cs_2AgBiCl_6$ X-ray detectors. And the photocurrent density of $Cs_2NaBiCl_6$, $Cs_3Bi_2Cl_9$, and $Cs_2AgBiCl_6$ X-ray detectors at different bias voltages and different dose rates X-ray irradiation.

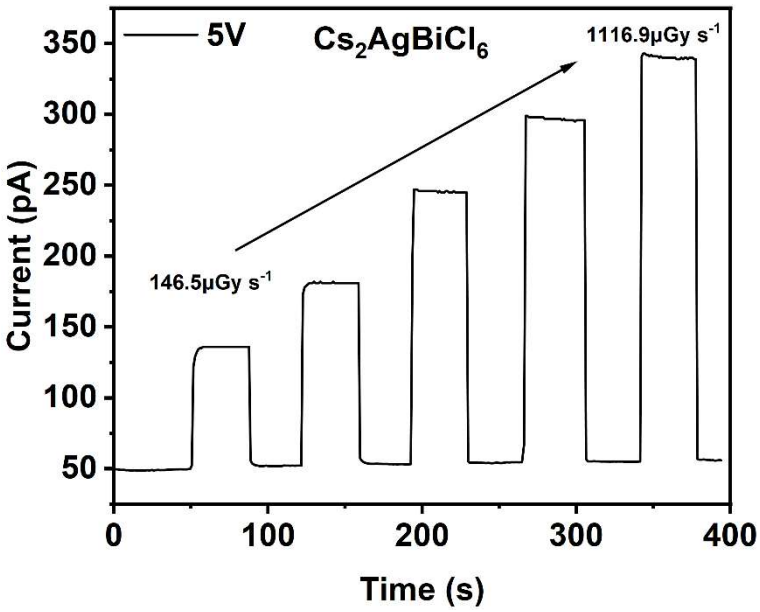

The I–T response curves of $Cs_2AgBiCl_6$ X-ray detectors at 5 V bias voltages and different dose rates X-ray irradiation (from 146.5 μGy s^{-1} to 1116.9 μGy s^{-1}).

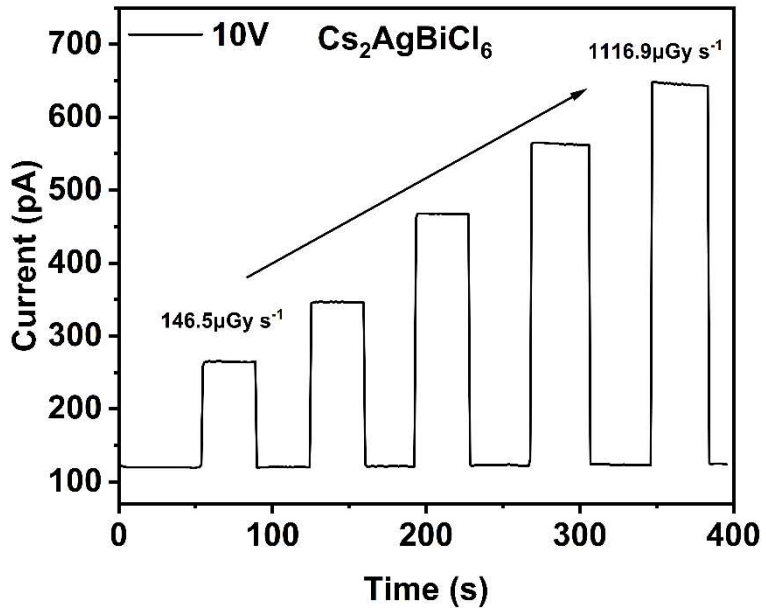

The I–T response curves of $Cs_2AgBiCl_6$ X-ray detectors at 10 V bias voltages and different dose rates X-ray irradiation (from 146.5 μGy s^{-1} to 1116.9 μGy s^{-1}).

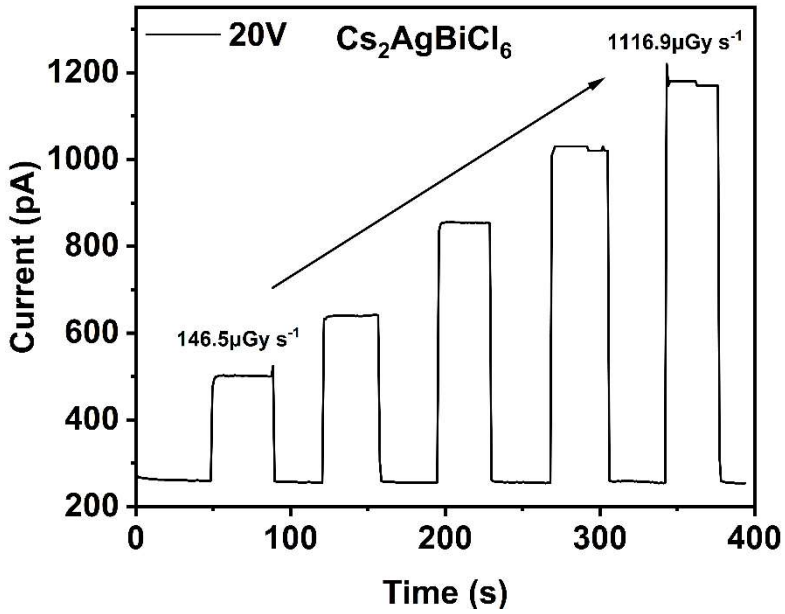

The I–T response curves of $Cs_2AgBiCl_6$ X-ray detectors at 20 V bias voltages and different dose rates X-ray irradiation (from 146.5 μGy s^{-1} to 1116.9 μGy s^{-1}).

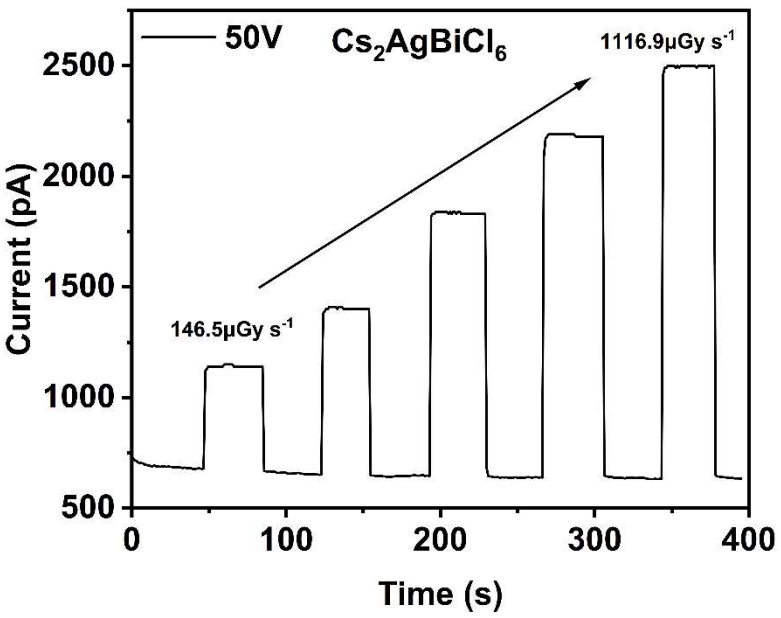

The I–T response curves of $Cs_2AgBiCl_6$ X-ray detectors at 50 V bias voltages and different dose rates X-ray irradiation (from 146.5 μGy s^{-1} to 1116.9 μGy s^{-1}).

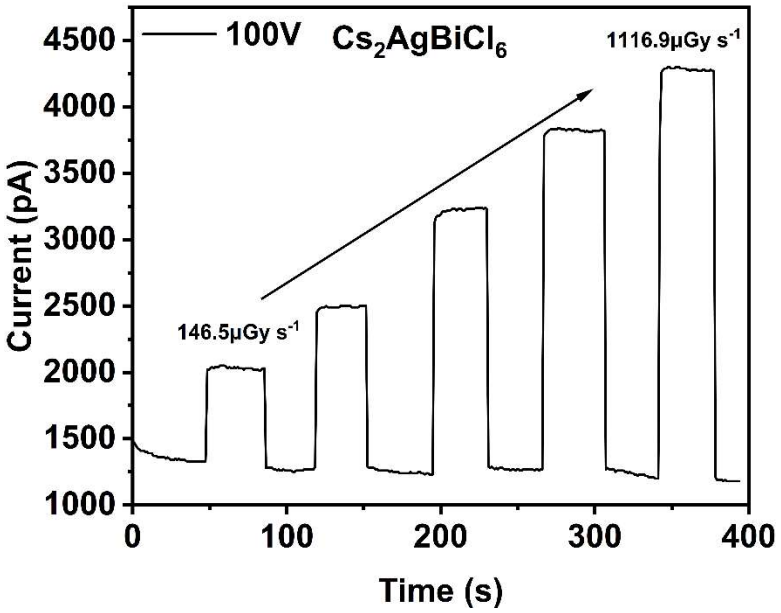

The I–T response curves of $Cs_2AgBiCl_6$ X-ray detectors at 100 V bias voltages and different dose rates X-ray irradiation (from 146.5 μGy s^{-1} to 1116.9 μGy s^{-1}).

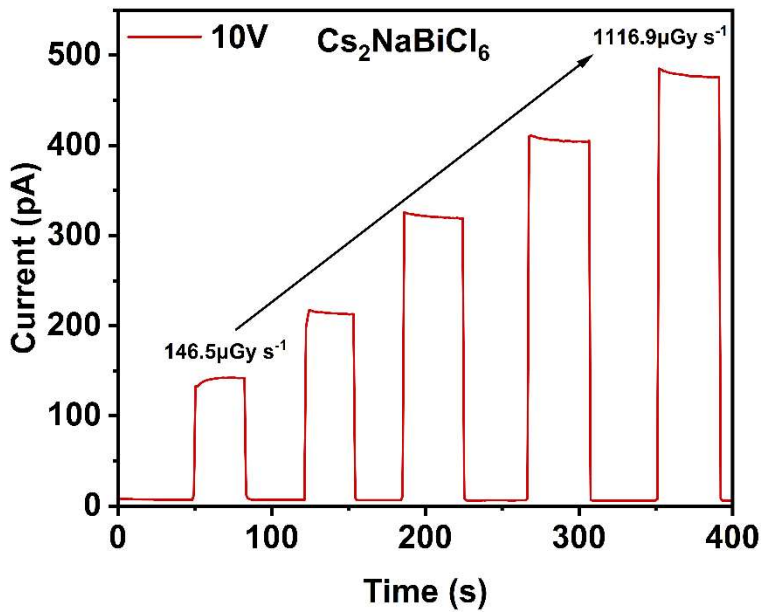

The I–T response curves of $Cs_2NaBiCl_6$ X-ray detectors at 10 V bias voltages and different dose rates X-ray irradiation (from 146.5 μGy s^{-1} to 1116.9 μGy s^{-1}).

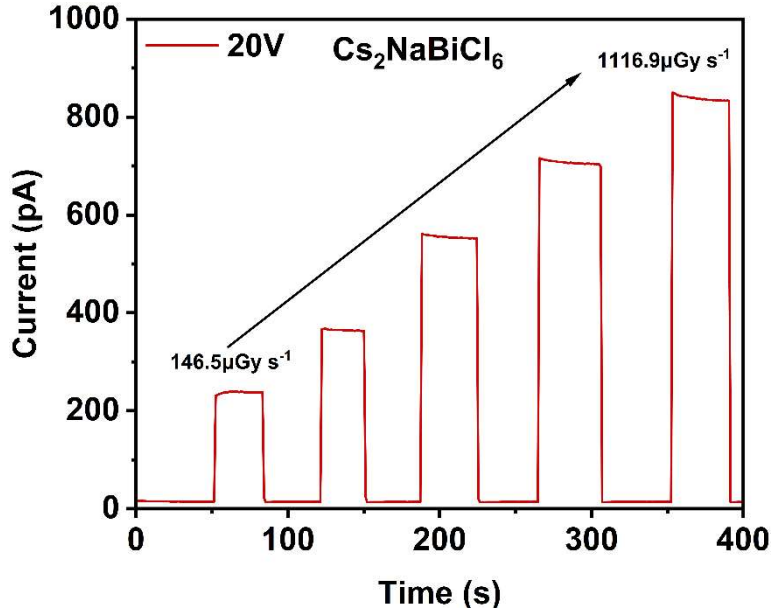

The I–T response curves of $Cs_2NaBiCl_6$ X-ray detectors at 20 V bias voltages and different dose rates X-ray irradiation (from 146.5 μGy s^{-1} to 1116.9 μGy s^{-1}).

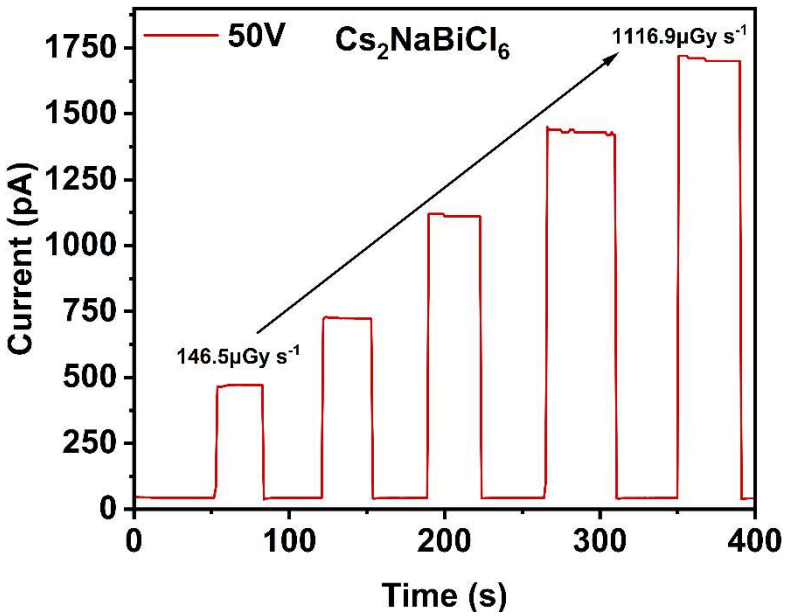

The I–T response curves of $Cs_2NaBiCl_6$ X-ray detectors at 50 V bias voltages and different dose rates X-ray irradiation (from 146.5 μGy s^{-1} to 1116.9 μGy s^{-1}).

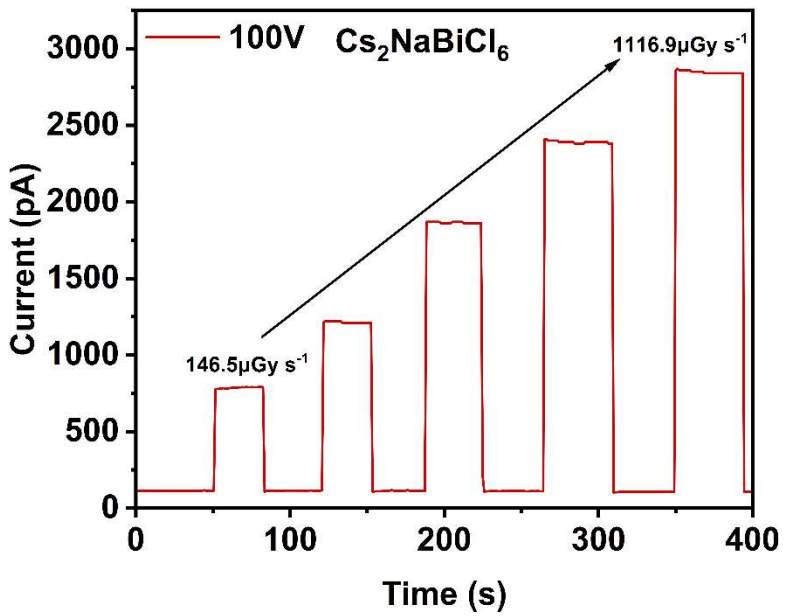

The I–T response curves of $Cs_2NaBiCl_6$ X-ray detectors at 100 V bias voltages and different dose rates X-ray irradiation (from 146.5 μGy s^{-1} to 1116.9 μGy s^{-1}).

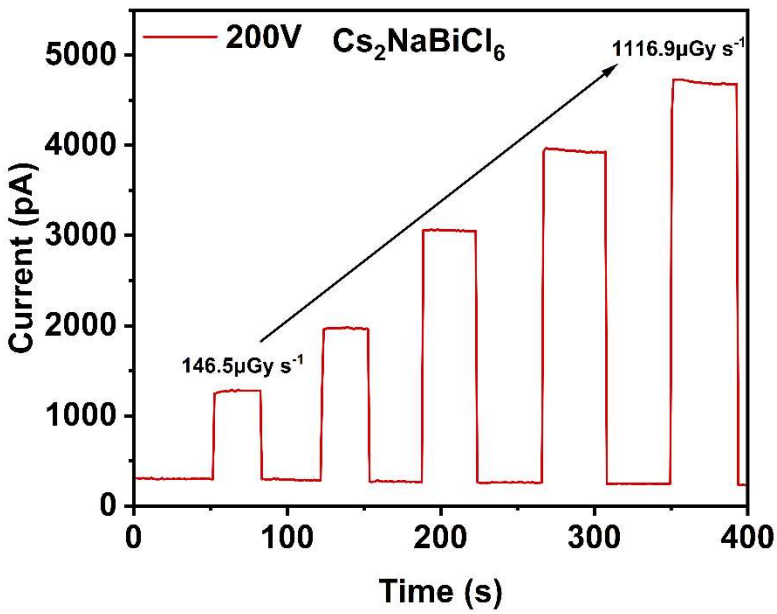

The I–T response curves of $Cs_2NaBiCl_6$ X-ray detectors at 200 V bias voltages and different dose rates X-ray irradiation (from 146.5 μGy s^{-1} to 1116.9 μGy s^{-1}).

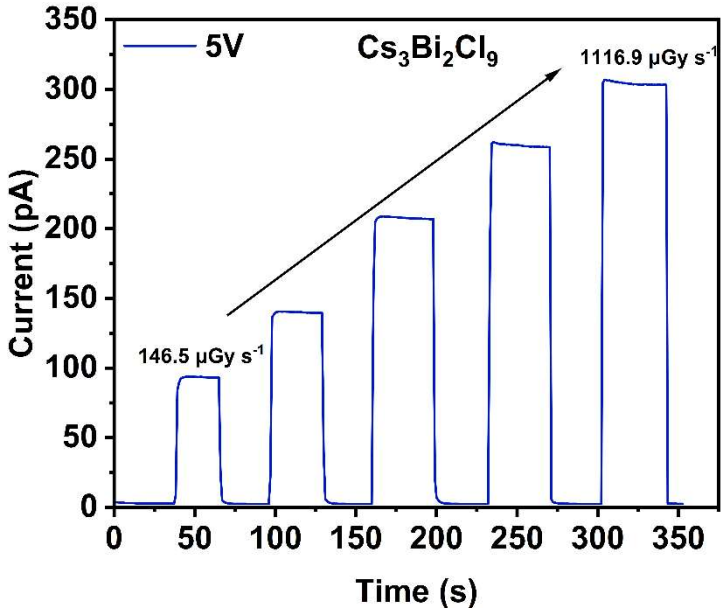

The I–T response curves of $Cs_2Bi_3Cl_9$ X-ray detectors at 5 V bias voltages and different dose rates X-ray irradiation (from 146.5 μGy s^{-1} to 1116.9 μGy s^{-1}).

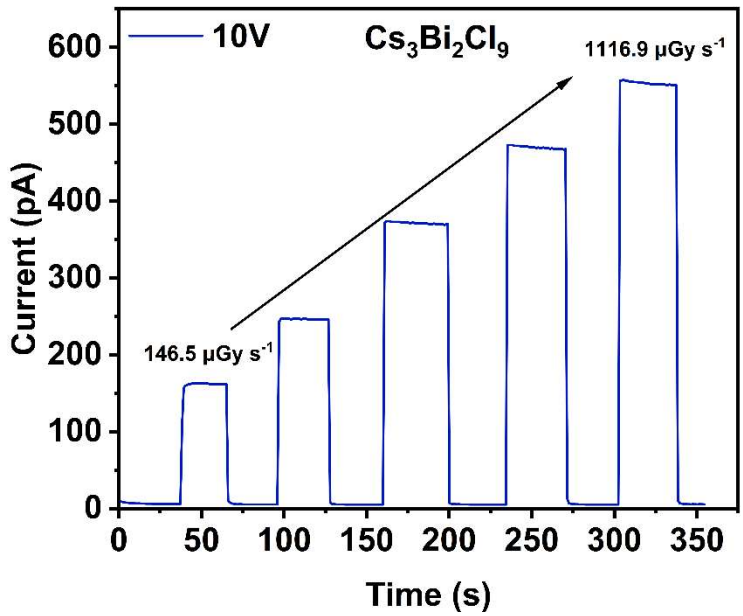

The I–T response curves of $Cs_2Bi_3Cl_9$ X-ray detectors at 10 V bias voltages and different dose rates X-ray irradiation (from 146.5 μGy s^{-1} to 1116.9 μGy s^{-1}).

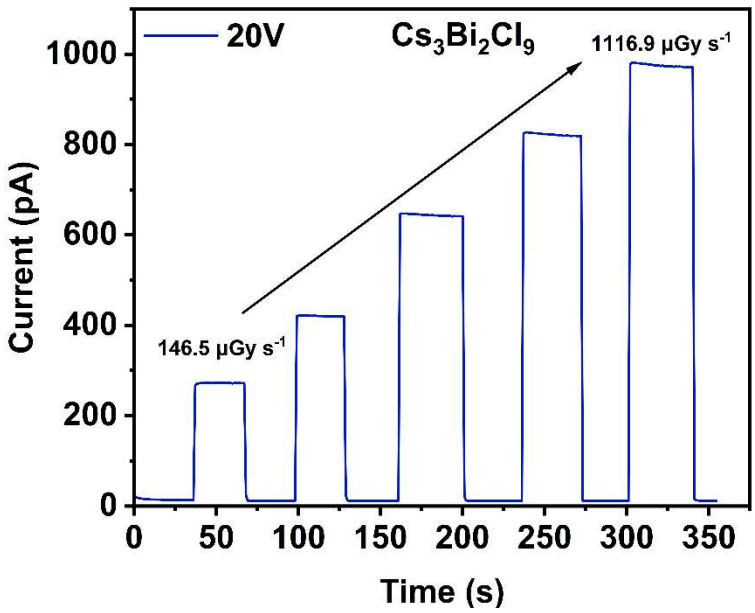

The I–T response curves of $Cs_2Bi_3Cl_9$ X-ray detectors at 20 V bias voltages and different dose rates X-ray irradiation (from 146.5 μGy s^{-1} to 1116.9 μGy s^{-1}).

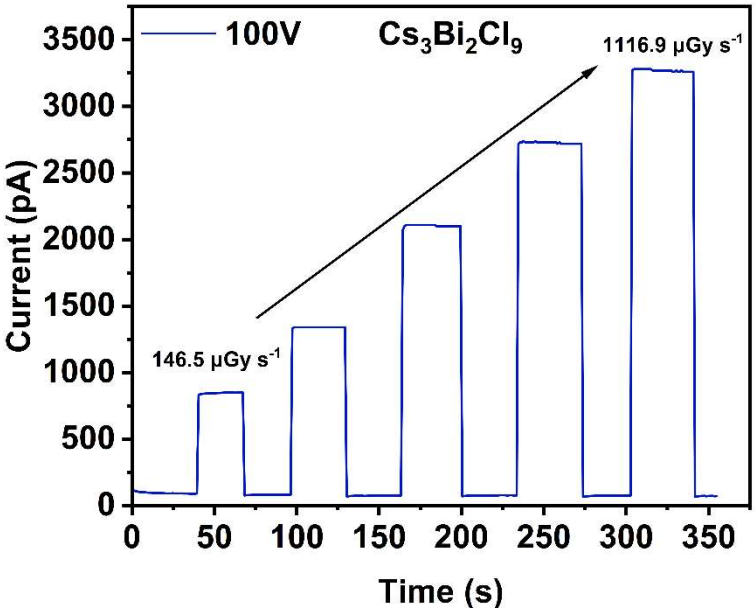

The I–T response curves of $Cs_2Bi_3Cl_9$ X-ray detectors at 100 V bias voltages and different dose rates X-ray irradiation (from 146.5 μGy s^{-1} to 1116.9 μGy s^{-1}).

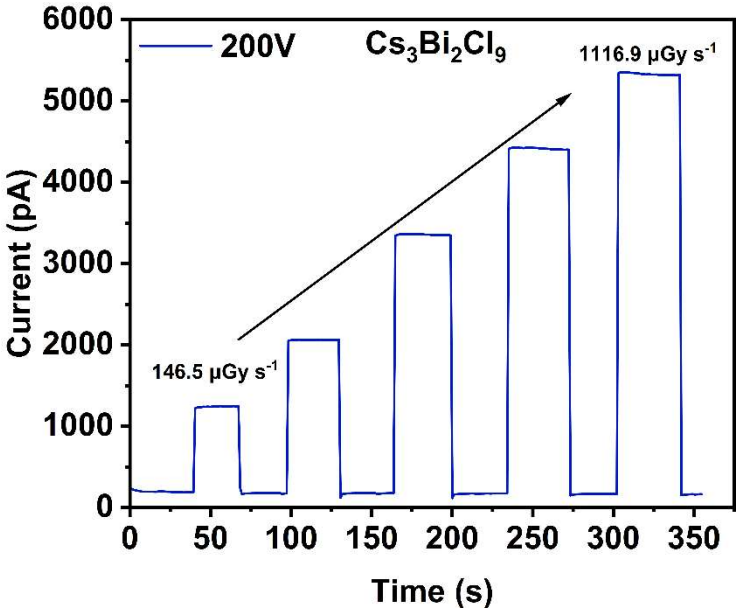

The I–T response curves of $Cs_2Bi_3Cl_9$ X-ray detectors at 200 V bias voltages and different dose rates X-ray irradiation (from 146.5 μGy s^{-1} to 1116.9 μGy s^{-1}).

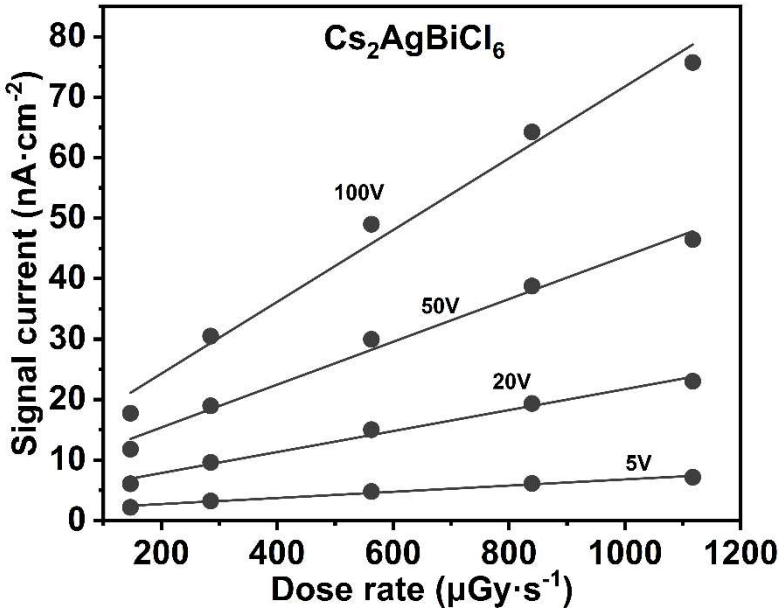

The photocurrent density of $Cs_2AgBiCl_6$ X-ray detectors at different bias voltages and different dose rates X-ray irradiation.

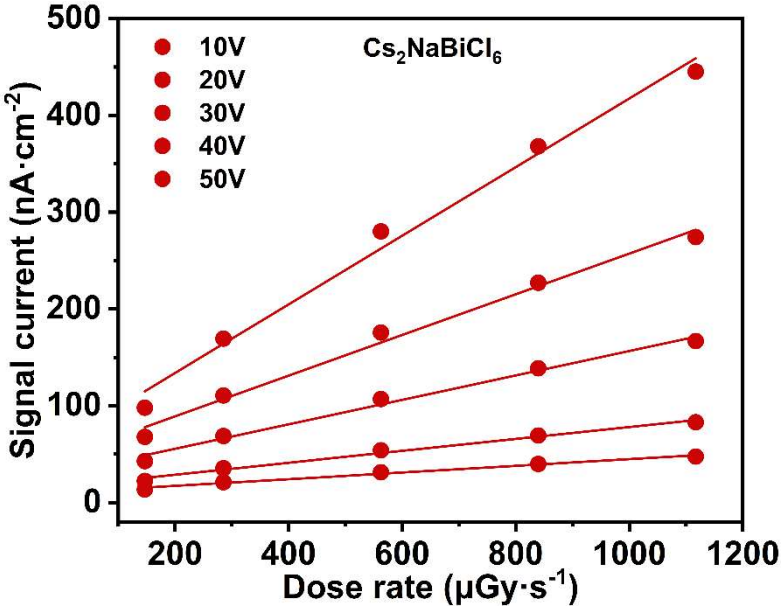

The photocurrent density of $Cs_2NaBiCl_6$ X-ray detectors at different bias voltages and different dose rates X-ray irradiation.

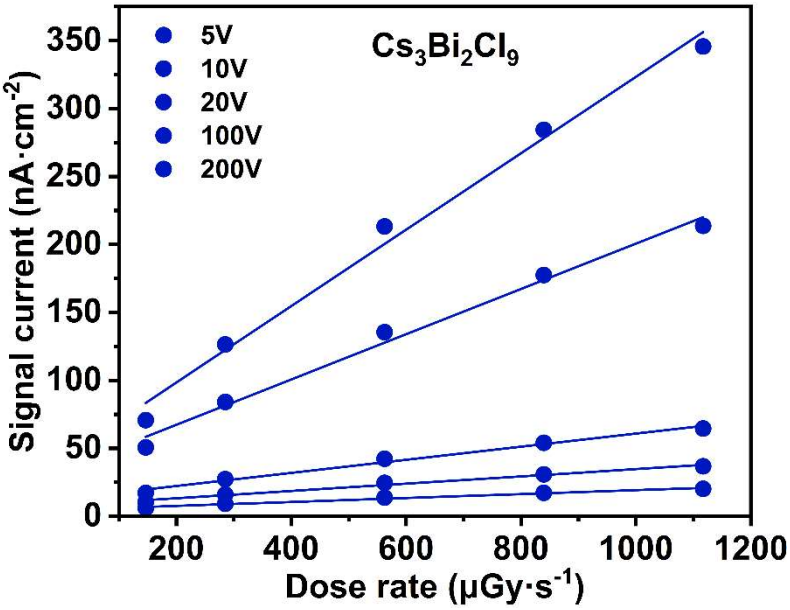

The photocurrent density of $Cs_3Bi_2Cl_9$ X-ray detectors at different bias voltages and different dose rates X-ray irradiation.

Figure S13. The dark and photo current of $Cs_2NaBiCl_6$, $Cs_3Bi_2Cl_9$, and $Cs_2AgBiCl_6$ X-ray detectors under different bias. All devices with gold as both electrodes showed a symmetric I–V curves, indicating that gold forms Ohmic contact with $Cs_2NaBiCl_6$, $Cs_3Bi_2Cl_9$, and $Cs_2AgBiCl_6$ single crystals.

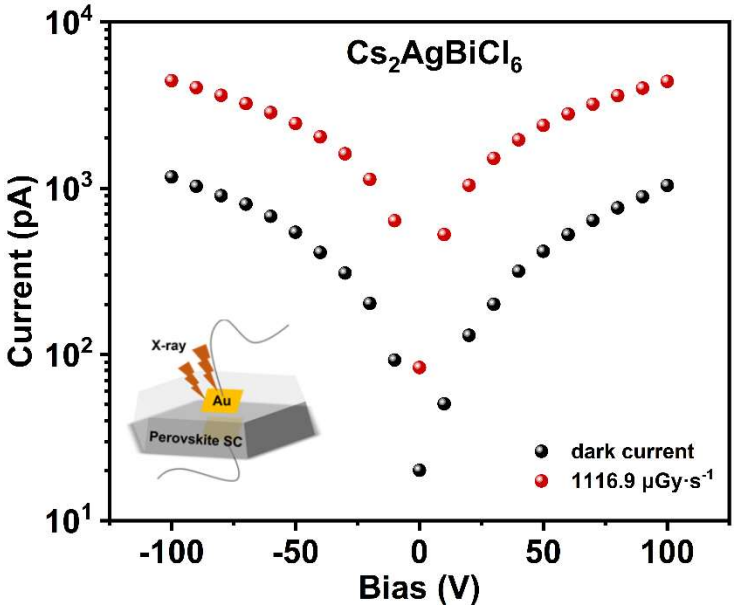

The symmetric I-V curve of $Cs_2AgBiCl_6$.

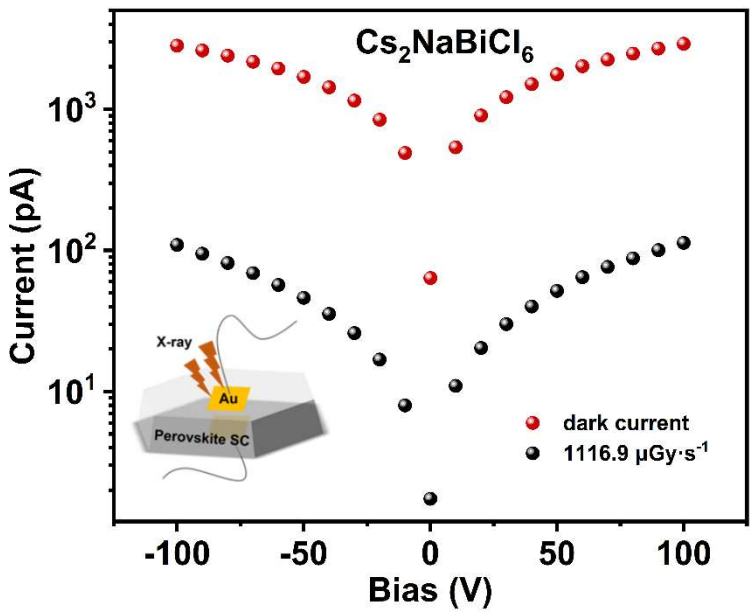

The symmetric I-V curve of $Cs_2AgBiCl_6$.

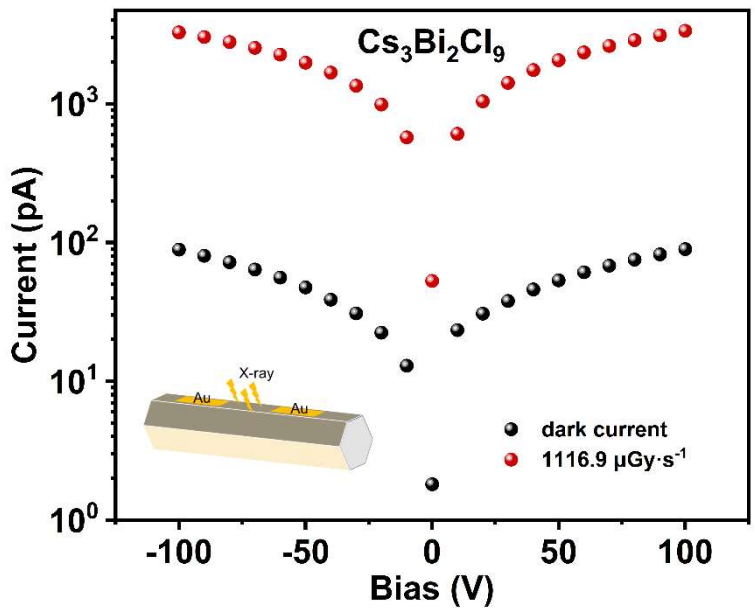

The symmetric I-V curve of $Cs_3Bi_2Cl_9$.

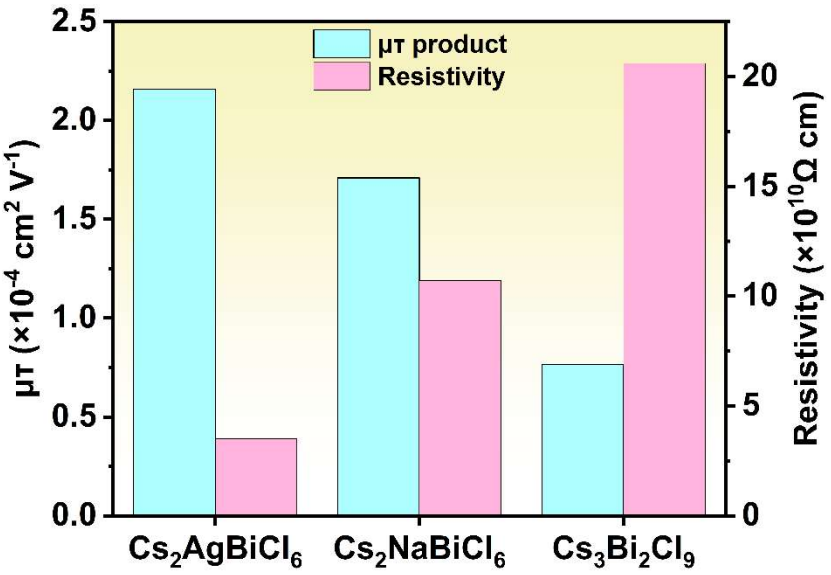

Figure S14. The carrier mobility-lifetime and resistivity of $Cs_2NaBiCl_6$, $Cs_3Bi_2Cl_9$, and $Cs_2AgBiCl_6$ X-ray detectors.

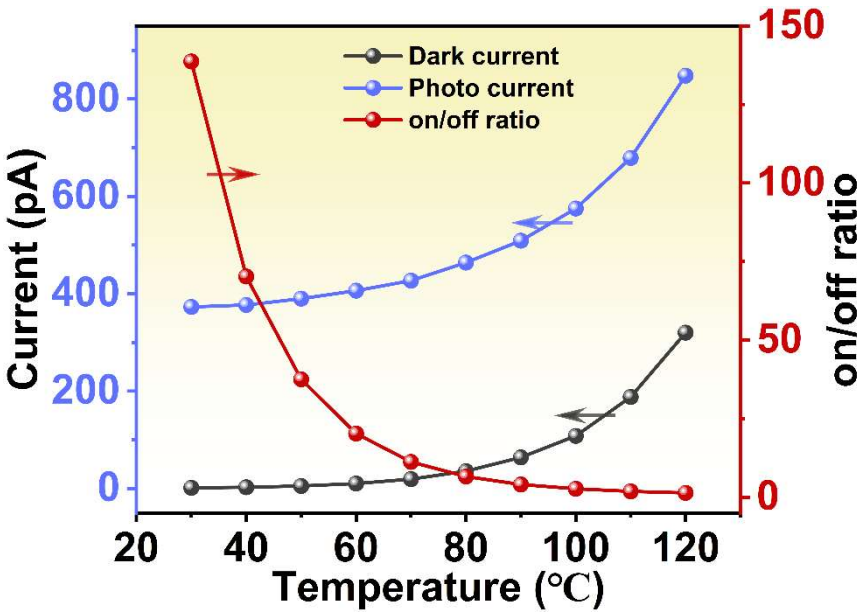

Figure S15. The dark and photo current response and on-off ratio of $Cs_2NaBiCl_6$ X-ray detectors between 30 °C and 120 °C. They show good thermal stability up to 50°C.

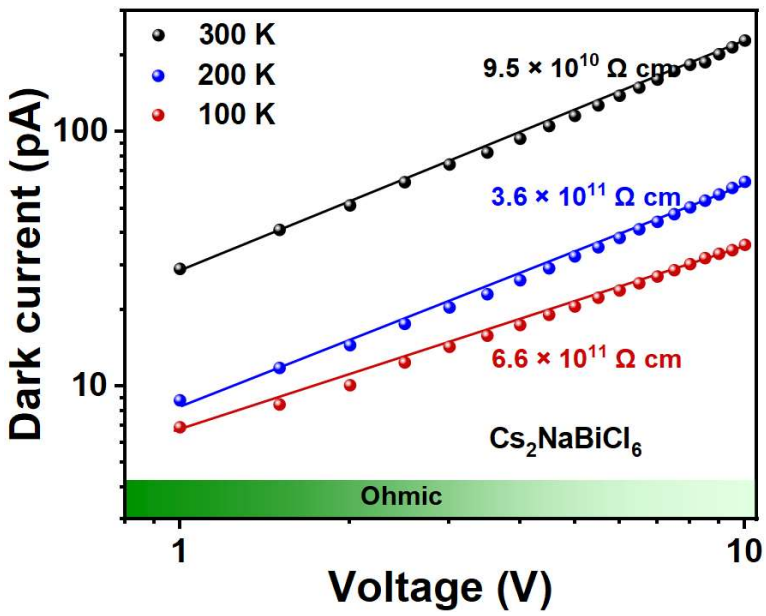

Figure S16. The dark I–V characterization performed on single-crystal $Cs_2NaBiCl_6$ device at 300, 200, and 100 K, respectively.

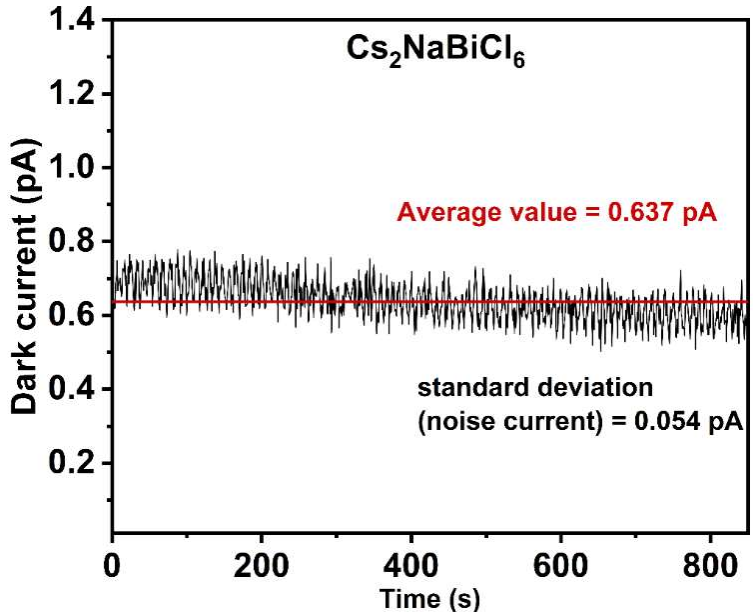

Figure S17. Extremely stable dark current of $Cs_2NaBiCl_6$ X-ray detectors at 10 voltages.

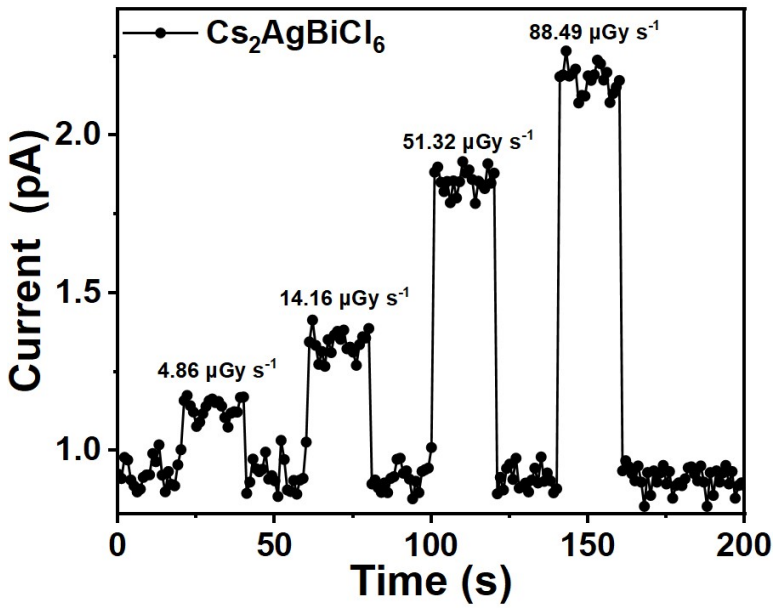
Cs2AgBiCl6
88.49 μGy s-1
51.32 μGy s-1
14.16 μGy s-1
4.86 μGy s-1
Current (pA)
2.0
1.5
1.0
0
50
100
150
200
Time (s)

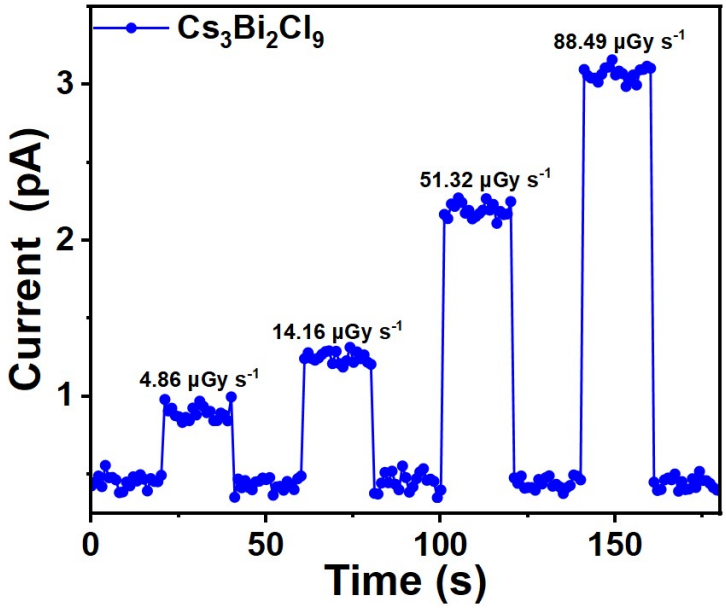
Cs3Bi2Cl9
88.49 μGy s-1
51.32 μGy s-1
14.16 μGy s-1
4.86 μGy s-1
Current (pA)
3
2
1
0
50
100
150
Time (s)

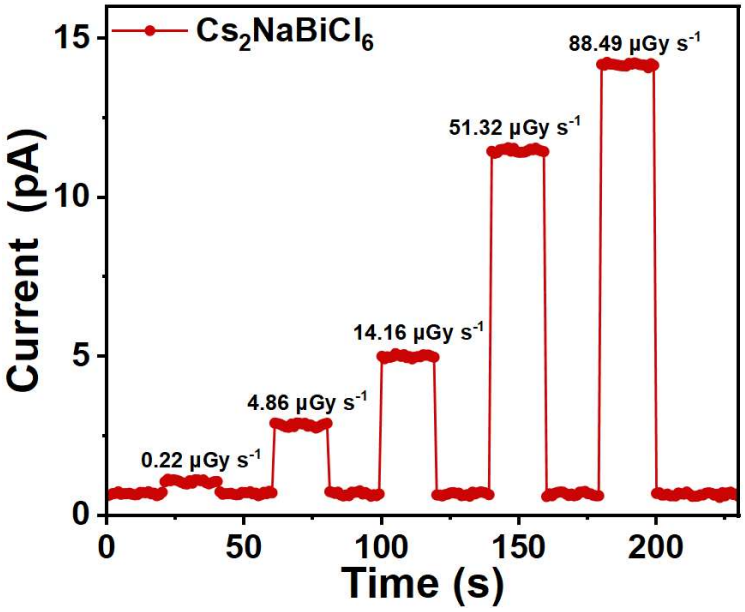

Figure S18. The I–T response curves of Cs2NaBiCl6, Cs3Bi2Cl9, and Cs2AgBiCl6 X-ray detectors at 10 V bias voltages and different dose rates X-ray irradiation.

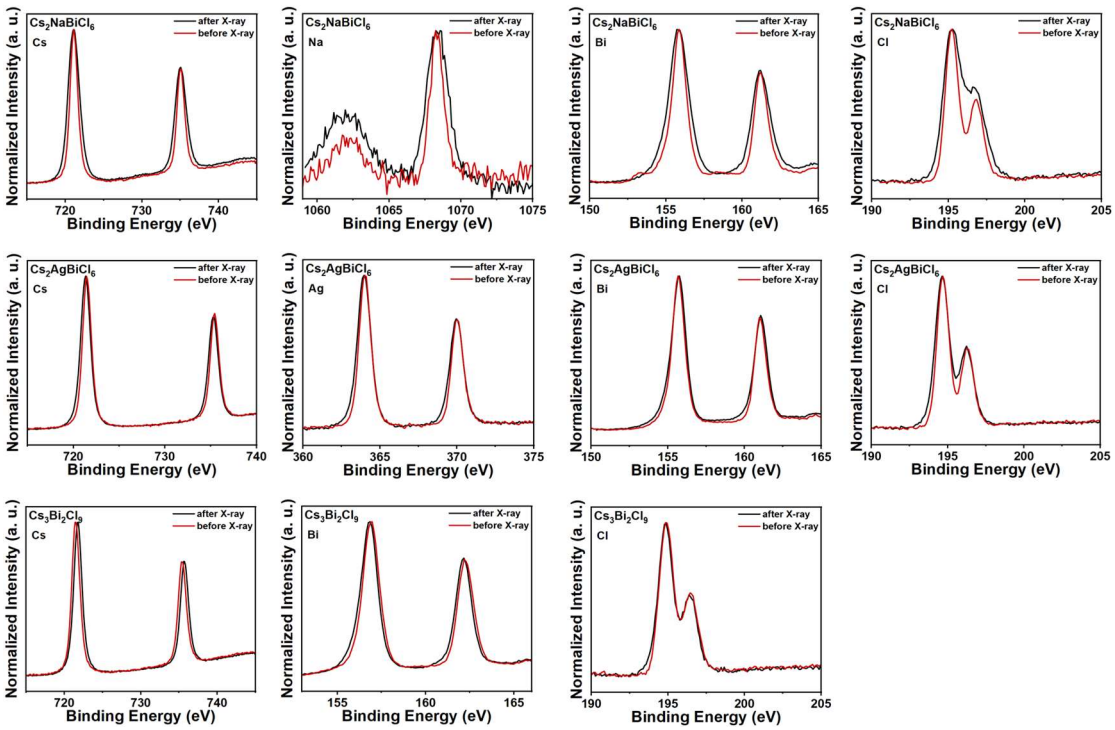

Figure S19. The XPS spectra of Cs, Ag, Na, Bi and Cl before and after irradiation of X-ray.

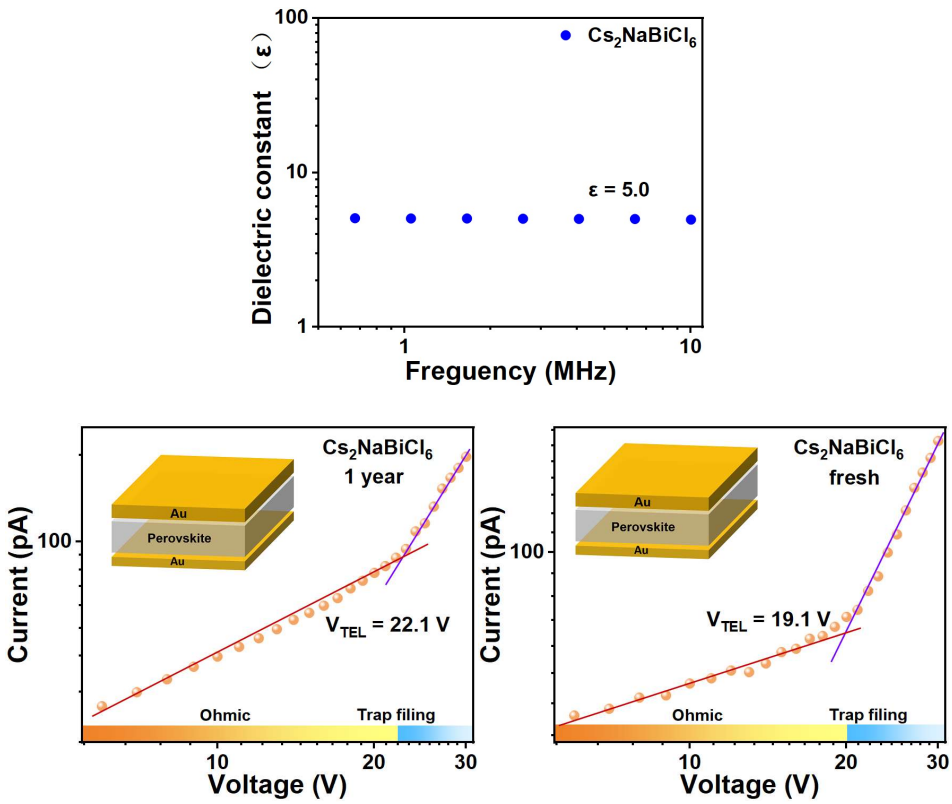

Figure S20. Frequency-dependent dielectric constant of the $Cs_2NaBiCl_6$ SCs. I-V curve of $Cs_2NaBiCl_6$ SC device from different times (inset: structure of the device used for measurement).

The ε is calculated to be 5 using an impedance analyzer. Then we evaluated the trap-state density of the $Cs_2NaBiCl_6$ SCs using a space-charge-limited current (SCLC) method. The current increased from the first linear ohmic region to the second trap-filled limited (TFL) region with increasing bias voltage, using the equation:

$$n_{trap} = \frac{2\varepsilon\varepsilon_0 V_{TFL}}{eL^2}$$

where n_{trap} refers to the trap density, VTFL is the trap-filled limit voltage, d is thickness, and e is the electron charge. The $Cs_2NaBiCl_6$ SC device shows a low trap density (n_{trap}) of 1.06×10^{10} cm^{-3}, which is beneficial for reduced carrier trapping. Further, we have calculated the mobility (μ) using the Mott−Gurney law. The μ value can be expressed as:

$$\mu = \frac{8Jd^3}{3\varepsilon\varepsilon_0 V^2}$$

where J is the dark current density, and V is the applied voltage. The mobility (μ) has

been estimated as 1.61×10^{-4} cm^2 V^{-1} s^{-1}.

Furthermore, $Cs_2NaBiCl_6$ SC devices are subjected to SCLC testing with a one-year time lag. It shows n_{trap} of 1.20×10^{10} cm^{-3}, which is only a 13 % improvement over the newly made device. And μ is valued as 1.24×10^{-4} cm^2 V^{-1} s^{-1}, which is reduced by 23% compared to freshly made devices. This demonstrates that $Cs_2NaBiCl_6$ SC devices have good stability.

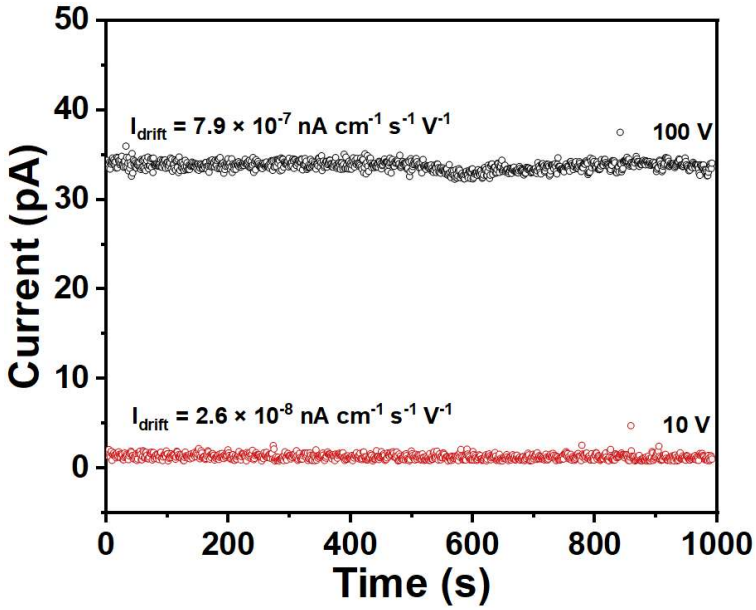

Figure S21. Dark current tracking of $Cs_2NaBiCl_6$ SC detector at 10 V and 100 V.

Table S6. The comparison of dark current stability among perovskite semiconductors.

Materials	Dimension	I_{drift} (nA cm^{-1} s^{-1} V^{-1})	Voltage	Ref.
$(MA)_3Bi_2I_9$	0D	5.0×10^{-10}	10 V	9
$(AG)_3Bi_2I_9$	0D	7.3×10^{-8}	200 V cm^{-1}	10
$(R/S\text{-}PPA)_2BiI_5$	1D	1.0×10^{-4}	10 V	11
$Cs_3Bi_2Br_9$	2D	2.8×10^{-10}	1000 V	12
$Rb_3Bi_2I_9$	2D	1.82×10^{-7}	100 V	13
$(R\text{-}MPA)_4AgBiI_8$	2D	1.0×10^{-3}	50 V	14
$(MA)PbI_3$	3D	2.0×10^{-3}	10 V	12
$CsPbBr_3$	3D	1.9×10^{-4}	200 V	15
$Cs_2AgBiBr_6$	3D	1.1×10^{-6}	—	12
$Cs_2NaBiCl_6$	3D	2.6×10^{-8}	10 V	This work
$Cs_2NaBiCl_6$	3D	7.9×10^{-7}	100 V	This work

Table S7. The 1D, double 2D and 3D bismuth-based perovskites for X-ray detection.

Materials	Dimension	Eg (eV)	Resistivity ($\times 10^{10}$ Ω cm)	μτ ($\times 10^{-4}$ cm^2 V^{-1})	Sensitivity (μC Gy^{-1} cm^{-2})	Lowest dose rate (nGys^{-1})	Ref.
$Cs_2AgBiBr_6$	3D	2.03	16	63 (after annealing) 37.5 (intrinsic)	105	59.7	16
$Cs_2AgBiCl_6$	3D	2.61	3.51	2.16	109.5	2424	This work
$Cs_2NaBiCl_6$	3D	3.42	10.7	1.71	354.5	59.4	This work
$(CPA)_4AgBiBr_8$	2D	—	—	10	0.8	—	17
$(BA)_2CsAgBiBr_7$	2D	2.38	15	12.1	4.2	—	18
$(I\text{-}BA)_4AgBiI_8$	2D	2.00	3.04	22.8	5.38	—	19
$(DFPIP)_4AgBiI_8$	2D	2.03	—	—	188	3130	20
$Cs_3Bi_2Cl_9$	1D	3.02	20.6	0.76	281.1	365	This work
$(H2MDAP)BiI_5$	1D	1.83	2.1	—	1.0	—	21
$(PDA)BiBr_5$	1D	2.71	21.3	126	3.8	—	22
$(DMEDA)BiI_5$	1D	1.86	—	—	72.5	—	23
$(BAH)BiI_4$	1D	1.77	42	1.95	1181.8	—	24
$Cs_3Bi_2I_9$	0D	1.95	1(100) 100(001)	0.203	111.9	—	25

Materials	Dimension	Eg (eV)	Resistivity ($\times 10^{10}$ Ω cm)	μτ ($\times 10^{-4}$ cm^2 V^{-1})	Sensitivity (μC Gy^{-1} cm^{-2})	Lowest dose rate ($nGys^{-1}$)	Ref.
$MA_3Bi_2I_9$	0D	1.98	3.74	28.7	1947	83	26
$FA_3Bi_2I_9$	0D	2.08	7.8	e: 1.3 h: 0.24	598.1	200	27
$(Gua)_3Bi_2I_9$	0D	2.08	39.4	—	8.23	237.54	28
$(AG)_3Bi_2I_9$	0D	1.95	3.78	79.4	5791	2.6	10
$(NH_4)_3Bi_2I_9$	2D	2.05	—	110	8000	Parallel: 210 perpendicular: 55	29
$Rb_3Bi_2I_9$	2D	1.89	23	25.1	159.7	8.32	13
$Cs_3Bi_2Br_9$	2D	2.61	68	0.37	230.4	—	12

Table S8. Single crystal X-ray diffraction data of three bismuth-chloride perovskites

Crystals	$Cs_3Bi_2Cl_9$	$Cs_2AgBiCl_6$	$Cs_2NaBiCl_6$
Empirical Formula	$Cs_3Bi_2Cl_9$	$Cs_2AgBiCl_6$	$Cs_2NaBiCl_6$
Formula Weight	1153.76	795.37	710.49
Temperature/K	294.2(4)	293(2)	296.5
Crystal System	Orthorhombic	Cubic	Cubic
Space group	Pnma	Fm-3m	Fm-3m
a/Å	18.6511(19)	10.7505(17)	10.8360(3)
b/Å	7.6228(7)	10.7505(17)	10.8360(3)
c/Å	13.1957(15)	10.7505(17)	10.8360(3)
α/°	90	90	90
β/°	90	90	90
γ/°	90	90	90
Volume/$Å^3$	1876.1(3)	1242.5(6)	1272.35(11)
Z	4	4	4
ρ_{calc} g/cm3	4.085	4.252	3.709
μ/mm-1	25.729	22.725	20.731
F(000)	1976	1368	1224
Crystal size/mm^3	0.1× 0.1 × 0.3	0.1× 0.1 × 0.4	0.02× 0.03 × 0.04
Radiation	Mo Kα (λ = 0.71073 Å)	Mo Kα (λ = 0.71073 Å)	Mo Kα (λ = 0.71073 Å)
2θ range for data collection/°	1.8430 to 29.5880	3.7340 to 29.6350	3.256 to 27.331
	-18≤ h ≤ 26	-8≤ h ≤ 10	-11≤ h ≤ 13
Index ranges	-7≤ k ≤ 10	-8≤ k≤ 14	-14≤ k ≤ 14
	-17≤ l ≤ 16	-3≤ l ≤ 13	-14≤ l ≤ 13
Reflections collected	6727	341	182
Data/restraints/parameters	2667/0/87	122/0/7	182/0/10
Goodness-of-fit on F^2	1.048	1.161	1.214
Final R indexes [I>=2σ (I)]	R_1 = 0.0888	R_1 = 0.0647	R_1 = 0.0185

	$wR_2 = 0.1362$	$wR_2 = 0.1417$	$wR_2 = 0.0430$
Final R indexes [all data]	$R_1 = 0.0616$	$R_1 = 0.0630$	$R_1 = 0.0185$
	$wR_2 = 0.1564$	$wR_2 = 0.1486$	$wR_2 = 0.0430$
Largest diff. peak/hole / e $Å^{-3}$	1.078/-2.155	1.783/-4.908	1.002/-1.511

References:

1. Tailor, N. K.; Maity, P.; Saidaminov, M. I.; Pradhan, N.; Satapathi, S., Dark Self-Healing-Mediated Negative Photoconductivity of a Lead-Free $Cs_3Bi_2Cl_9$ Perovskite Single Crystal. *The Journal of Physical Chemistry Letters* **2021,** *12* (9), 2286-2292.

2. Majher, J. D.; Gray, M. B.; Strom, T. A.; Woodward, P. M., $Cs_2NaBiCl_6$:Mn^{2+}—A New Orange-Red Halide Double Perovskite Phosphor. *Chemistry of Materials* **2019,** *31* (5), 1738-1744.

3. McClure, E. T.; Ball, M. R.; Windl, W.; Woodward, P. M., Cs_2AgBiX_6 (X = Br, Cl): New Visible Light Absorbing, Lead-Free Halide Perovskite Semiconductors. *Chemistry of Materials* **2016,** *28* (5), 1348-1354.

4. Wang, M.; Zeng, P.; Wang, Z.; Liu, M., Vapor-Deposited $Cs_2AgBiCl_6$ Double Perovskite Films toward Highly Selective and Stable Ultraviolet Photodetector. *Advanced Science* **2020,** *7* (11), 1903662.

5. Li, H.; Pi, C.; Chen, W.; Zhou, M.; Wei, J.; Yi, J.; Song, P.; Alexey, Y.; Zhong, Y.; Yu, X.; Qiu, J.; Xu, X., A Highly Stable Photodetector Based on a Lead-Free Double Perovskite Operating at Different Temperatures. *The Journal of Physical Chemistry Letters* **2021,** *12* (24), 5682-5688.

6. Nandigana, P.; Pari, S.; Sujatha, D.; Shidhin, M.; Jeyabharathi, C.; Panda, S. K., Lead-Free Bismuth-Based Halide Perovskites with Excellent Stability for Visible-light-Driven Photoelectrochemical Water Splitting. *ChemistrySelect* **2023,** *8* (4), e202204731.

7. Yao, F.; Li, R.; Jia, Z.; Bai, S.; Yang, Y.; Li, Y.; Xu, Y.; Fang, G.; Lin, Q., Charge-Carrier Dynamics of Evaporated Bismuth-Based Chalcogenide Thin Films Probed with Time-Resolved Microwave Conductivity. *The Journal of Physical Chemistry Letters* **2023,** *14* (24), 5517-5523.

8. Steele, J. A.; Puech, P.; Keshavarz, M.; Yang, R.; Banerjee, S.; Debroye, E.; Kim,

C. W.; Yuan, H.; Heo, N. H.; Vanacken, J.; Walsh, A.; Hofkens, J.; Roeffaers, M. B. J., Giant Electron–Phonon Coupling and Deep Conduction Band Resonance in Metal Halide Double Perovskite. *ACS Nano* **2018,** *12* (8), 8081-8090.

9 Yucheng Liu, Zhuo Xu, Zhou Yang, Yunxia Zhang, Jian Cui, Yihui He, Haochen Ye, Kui Zhao, Huaming Sun, Rui Lu, Ming Liu, Mercouri G. Kanatzidis, and Shengzhong (Frank) Liu., Inch-Size 0D-Structured Lead-Free Perovskite Single Crystals for Highly Sensitive Stable X-Ray Imaging. *Matter* **2020,** 3, 180–196.

10 Ming Chen, Xiaofeng Dong, Depeng Chu, Binxia Jia, Xiaojie Zhang, Zeqin Zhao, Jinglu Hao, Yunxia Zhang, Jiangshan Feng, Xiaodong Ren, Yuqian Liang, Ruixin Shi, Adel Najar, Yucheng Liu, Shengzhong (Frank) Liu., Interlayer-Spacing Engineering of Lead-Free Perovskite Single Crystal for High-Performance X-ray Imaging. *Advanced Materials* **2023,** 35(18), 2211977.

11 Shihai You, Zeng-Kui Zhu, Shuheng Dai, Jianbo Wu, Qianwen Guan, Tingting Zhu, Panpan Yu, Changjian Chen, Qiushui Chen, Junhua Luo., Inch-Size Single Crystals of Lead-Free Chiral Perovskites with Bulk Photovoltaic Effect for Stable Self-Driven X-Ray Detection. *Advanced Functional Materials* **2023,** 33(36), 2303523.

12 Xiang LiPeng ZhangYunqiu HuaFucai CuiXue SunLin LiuYanxiao BiZhongjie YueGuodong Zhang and Xutang Tao,. Ultralow Detection Limit and Robust Hard X-ray Imaging Detector Based on Inch-Sized Lead-Free Perovskite Cs3Bi2Br9 Single Crystals. *ACS Appl. Mater. Interfaces* **2022**, 14, 9340−9351.

13 Mengling Xia, Jun-Hui Yuan, Guangda Niu,* Xinyuan Du, Lixiao Yin, Weicheng Pan, Jiajun Luo, Zhigang Li, Hongtao Zhao, Kan-Hao Xue, Xiangshui Miao, and Jiang Tang., Unveiling the Structural Descriptor of A3B2X9 Perovskite Derivatives toward X-Ray Detectors with Low Detection Limit and High Stability. *Advanced Functional Materials* **2020,** 30, 1910648.

14 Jian bo, Wu Shihai You, Junhua Luo., Chirality Inducing Polar Photovoltage in a

2D Lead-Free Double Perovskite toward Self-Powered X-ray Detection. *ACS Energy Lett.* **2023**, 8(6), 2809–2816.

15 Yihui He, Matthew Petryk, Zhifu Liu, Daniel G. Chica, Mercouri G. Kanatzidis., CsPbBr3 perovskite detectors with 1.4% energy resolution for high-energy γ-rays. *Nature Photonics* **2021**, 15, 36–42.

16. Pan, W.; Wu, H.; Luo, J.; Deng, Z.; Ge, C.; Chen, C.; Jiang, X.; Yin, W.-J.; Niu, G.; Zhu, L.; Yin, L.; Zhou, Y.; Xie, Q.; Ke, X.; Sui, M.; Tang, J., $Cs_2AgBiBr_6$ single-crystal X-ray detectors with a low detection limit. *Nature Photonics* **2017,** *11* (11), 726-732.

17. Guo, W.; Liu, X.; Han, S.; Liu, Y.; Xu, Z.; Hong, M.; Luo, J.; Sun, Z., Room-Temperature Ferroelectric Material Composed of a Two-Dimensional Metal Halide Double Perovskite for X-ray Detection. *Angewandte Chemie International Edition* **2020,** *59* (33), 13879-13884.

18. Xu, Z.; Liu, X.; Li, Y.; Liu, X.; Yang, T.; Ji, C.; Han, S.; Xu, Y.; Luo, J.; Sun, Z., Exploring Lead-Free Hybrid Double Perovskite Crystals of $(BA)_2CsAgBiBr_7$ with Large Mobility-Lifetime Product toward X-Ray Detection. *Angewandte Chemie International Edition* **2019,** *58* (44), 15757-15761.

19. Xu, Z.; Wu, H.; Li, D.; Wu, W.; Li, L.; Luo, J., A lead-free I-based hybrid double perovskite $(I\text{-}C_4H_8NH_3)_4AgBiI_8$ for X-ray detection. *Journal of Materials Chemistry C* **2021,** *9* (38), 13157-13161.

20. Wang, C. F.; Li, H.; Li, M. G.; Cui, Y.; Song, X.; Wang, Q. W.; Jiang, J. Y.; Hua, M. M.; Xu, Q.; Zhao, K.; Ye, H. Y.; Zhang, Y., Centimeter-Sized Single Crystals of Two-Dimensional Hybrid Iodide Double Perovskite (4,4-Difluoropiperidinium)$_4AgBiI_8$ for High-Temperature Ferroelectricity and Efficient X-Ray Detection. *Advanced Functional Materials* **2021,** *31* (13), 2009457.

21. Tao, K.; Li, Y.; Ji, C.; Liu, X.; Wu, Z.; Han, S.; Sun, Z.; Luo, J., A Lead-Free Hybrid Iodide with Quantitative Response to X-ray Radiation. *Chemistry of Materials* **2019,** *31* (15), 5927-5932.

22. Xu, Y.; Hu, J.; Du, X.; Xiao, X.; Li, M.; Tang, J.; Chen, J.; He, Y., Antisolvent-assisted Crystallization of Centimeter-sized Lead-free Bismuth Bromide Hybrid Perovskite Single Crystals with X-ray Sensitive Merits. *Chemistry-An Asian Journal* **2021,** *16* (24), 4137-4144.

23. Yao, L.; Niu, G.; Yin, L.; Du, X.; Lin, Y.; Den, X.; Zhang, J.; Tang, J., Bismuth halide perovskite derivatives for direct X-ray detection†. *Journal of Materials Chemistry C* **2019,** *8* (4), 1239-1243.

24. Ma, C.; Li, H.; Chen, M.; Liu, Y.; Zhao, K.; Liu, S., Water-Resistant Lead-Free Perovskitoid Single Crystal for Efficient X-Ray Detection. *Advanced Functional Materials* **2022,** *32* (30), 220216013.

25. Yucheng Liu, Zhuo Xu, Zhou Yang, Yunxia Zhang, Jian Cui, Yihui He, Haochen Ye, Kui Zhao, Huaming Sun, Rui Lu, Ming Liu, Mercouri G. Kanatzidis, and Shengzhong (Frank) Liu., Inch-Size 0D-Structured Lead-Free Perovskite Single Crystals for Highly Sensitive Stable X-Ray Imaging. *Matter* **2020**, 3, 180–196.

26. Yunxia Zhang, Yucheng Liu, Zhuo Xu, Haochen Ye, Zhou Yang, Jiaxue You, Ming Liu, Yihui He, Mercouri G. Kanatzidis & Shengzhong (Frank) Liu., Nucleation-controlled growth of superior lead-free perovskite Cs3Bi2I9 single-crystals for high-performance X-ray detection. *Nature Communications* **2020**, 11, 2304.

27. Wei Li, Deyu Xin,Shujie Tie, Jiwei Ren, Siyin Dong, Lin Lei, Xiaojia Zheng, Yiying Zhao, Wen-Hua Zhang., Zero Dimensional Lead Free FA3Bi2I9 Single Crystals for High Performance X-ray Detection. *J. Phys. Chem. Lett.* **2021**, 12, 7, 1778–1785.

28. Yaxin Xu, Jiarui Hu, Xingfu Xiao, Huanfeng He, Guoliang Tong, Junnian Chen and Yunbin He., Evaporation crystallization of zero-dimensional guanidinium bismuth iodide perovskite single crystal for X-ray detection. *Inorg. Chem. Front.*, **2022**, 9, 494.

29. Renzhong Zhuang, Xueji Wang, Wenbo Ma, Haiming Zhu, Yuhao Wu 1, Xu Chen, Longhua Tang, Jiyong Liu, Lingling Wu, Wei Zhou, Xu Liu and Yang (Michael) Yang., Highly sensitive X-ray detector made of layered perovskite-like (NH4)3Bi2I9 single crystal with anisotropic response. *Nature Photonics*, **2019**, 13, 602–608.